



Original Paper

Application of Land Magnetic and Geoelectrical Techniques for Delineating Groundwater Aquifer: Case Study in East Oweinat, Western Desert, Egypt

Sultan Awad Sultan Araffa^{1,3} and Sayed Bedair²

Received 21 May 2021; accepted 12 August 2021
Published online: 26 August 2021

Two geophysical tools were used to delineate the configuration of the Nubian sandstone aquifer in the study area. Three hundred magnetic points were measured and analyzed to evaluate the subsurface structural setting and to trace the basement relief, which control the aquifer's geometry. The magnetic interpretations refer to dominant faults that strike in various directions, namely N–S, NE–SW, and NW–SE. The top of the basement complex was recorded at depths of 384–1286 m, and the aquifer thickness ranged from 299 to 1169 m. Thirty vertical electrical sounding points of AB/2 with depths ranging from 1.5 to 700 m were used to estimate the parameters of the Nubian sandstone aquifer. The geoelectrical data indicate that the area consists of 5 units; the first unit is composed of sand and gravel, the second unit of ferruginous sandstone, the third unit of clay, the fourth unit of dry sandstone, and the last unit of sandstone saturated with groundwater. The groundwater in the study area is freshwater of high quality usable for all purposes.

KEY WORDS: Groundwater, Vertical electrical sounding, Land magnetic, Faults, Basement complex.

INTRODUCTION

The area represents the main source of water for cultivated land where the depth of fresh groundwater is shallow and most of the surface layer (soil) is suitable for agriculture. The surface layer consists of silty clay, which is rich with mineral elements that are important for agricultural projects. The study area is located between 22° 08' and 22° 20' N latitudes and between 29° 00' and 29° 35' E longitudes (Fig. 1a); it covers an area of 652 km²

(Fig. 1b). It lies near the Egypt–Sudan border, and it is untainted and unpolluted. No extensive geophysical investigations have been carried out in this area; however, many studies have been conducted previously northward and eastward from the study area. Masoud et al. (2013) studied the configuration of the Nubian sandstone aquifer and concluded that the main recharging source of this aquifer in the south Western Desert is the underground inflow coming across the southern boundary of Egypt. El Osta (2006) evaluated the management of groundwater in East El Oweinat area. Goldman and Neubauer (1994) used integrated geophysical techniques for groundwater exploration. According to Al Temamy and Barseem (2010), the study area and its surroundings are characterized by wide diurnal variations, arid climates, and high temperatures. Maximum temperature values are recorded during

¹National Research Institute of Astronomy and Geophysics, Helwan, Cairo 11722, Egypt.

²National Water Research Center (NWRC), Research Institute for Ground Water (RIGW), Cairo, Egypt.

³To whom correspondence should be addressed; e-mail: sultan_awad@yahoo.com

June (40 °C), while minimum values are recorded during December (5.2 °C). Evaporation is maximum during June (32.8 mm/day) and minimum in January (5.4 mm/day).

The present authors recently used different geoscience data such as electrical resistivity, land magnetic, and well-logging data to establish the Nubian aquifer. Examples of our previous recent studies include the following. Araffa (2013) and Araffa et al. (2015) applied different geophysical tools for groundwater exploration. Araffa et al. (2020) and El-Badrawy et al. (2021) investigated the occurrences and disruption of groundwater at the Wadi Hagul area and central Sinai, respectively. Elbarbary et al. (2021) studied the potentiality of groundwater at the northern part of Sinai. Araffa et al. (2021) defined the Moghra aquifer using well-logging and geophysical data. This present work aimed to delineate the groundwater aquifer, define the basement surface and subsurface structures that control the groundwater aquifer's configuration, and to determine the water quality from resistivity values after converting these to electrical conductivity, and finally estimate the total dissolved salts (TDS) in ppm.

GEOLOGY OF THE AREA UNDER STUDY

According to Issawi (1971, 1973) and Klitzsch (1978), Klitzsch and Lejal-Nicol (1984), basement rocks outcrop east of El Oweinat near the study area at Qaret El-Mayet and they are overlain by Upper Cretaceous and Quaternary rocks. Hendriks et al. (1987) indicated that the pre-Maastrichtian Nubia Group overlies the Precambrian basement. Near the basement rock, at Qaret El-Mayet, the Nubian sandstone is intensively ferruginated. The Upper Cretaceous rocks are represented by Nubian sandstone exposures forming isolated hills. Most of the study area occupied by Nubian sandstone consists of different formations such as the Six Hill Formation of Lower Cretaceous. The Lower–Upper Cretaceous Sabeya Formation covers the northern portion, while the Lower Cretaceous Kissiba Formation occupies the northeastern portion (Fig. 1b). The Quaternary deposits in the area under study are differentiated into gravelly sheets, sands, sand sheets, and sand dunes. Attia and Hussien (2015) concluded that the areas surrounding the study area are covered with Lower Cretaceous to Quaternary rock formations. The Quaternary units are com-

Figure 1. (a) Index map showing location of the study area. (b) Surface geologic map of the study area (modified from Conoco, 1987).

posed of playa, sabkha, salt, aeolian sand, and sand accumulations.

The geological setting was correlated with a borehole (21R) drilled about 30 km from the study area. The borehole 21R was drilled at 22° 37' 19.5" N latitude and 28° 37' 58.2" E longitude to a depth of 294 m. The description of this borehole indicates that the lithology consists of sandstone comprising a thickness of about 7.5 m, an overlay clay of 15 m thickness, sandstone intercalated with clay to a depth of 290 m, and basement rocks at 290–294 m depth (Fig. 2).

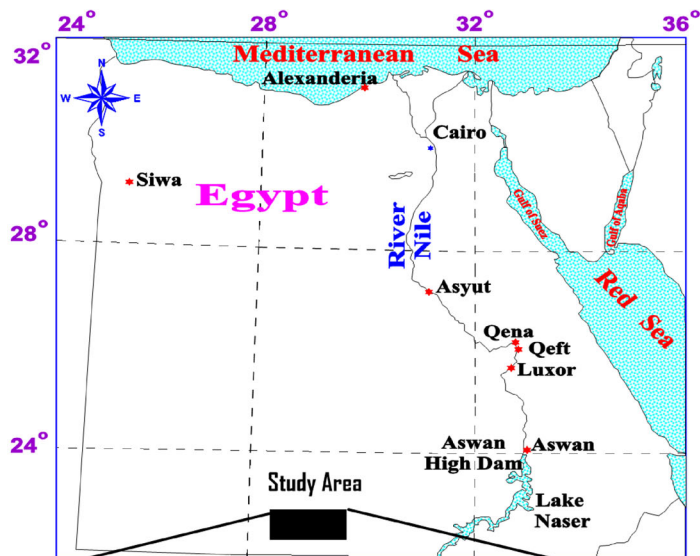
METHODOLOGY

Two geophysical tools were used to delineate the aquifer parameters. The first tool is land magnetic survey to detect faults and the topography of the basement complex, which controls the groundwater aquifer. The second tool is vertical electrical sounding (VES) to characterize the aquifer geometry, including depth to water, aquifer thickness, and lithological characteristics of the water-bearing formation. This exploration program dealt with mapping of the Nubian aquifer and the delineation of faults in the bedrock.

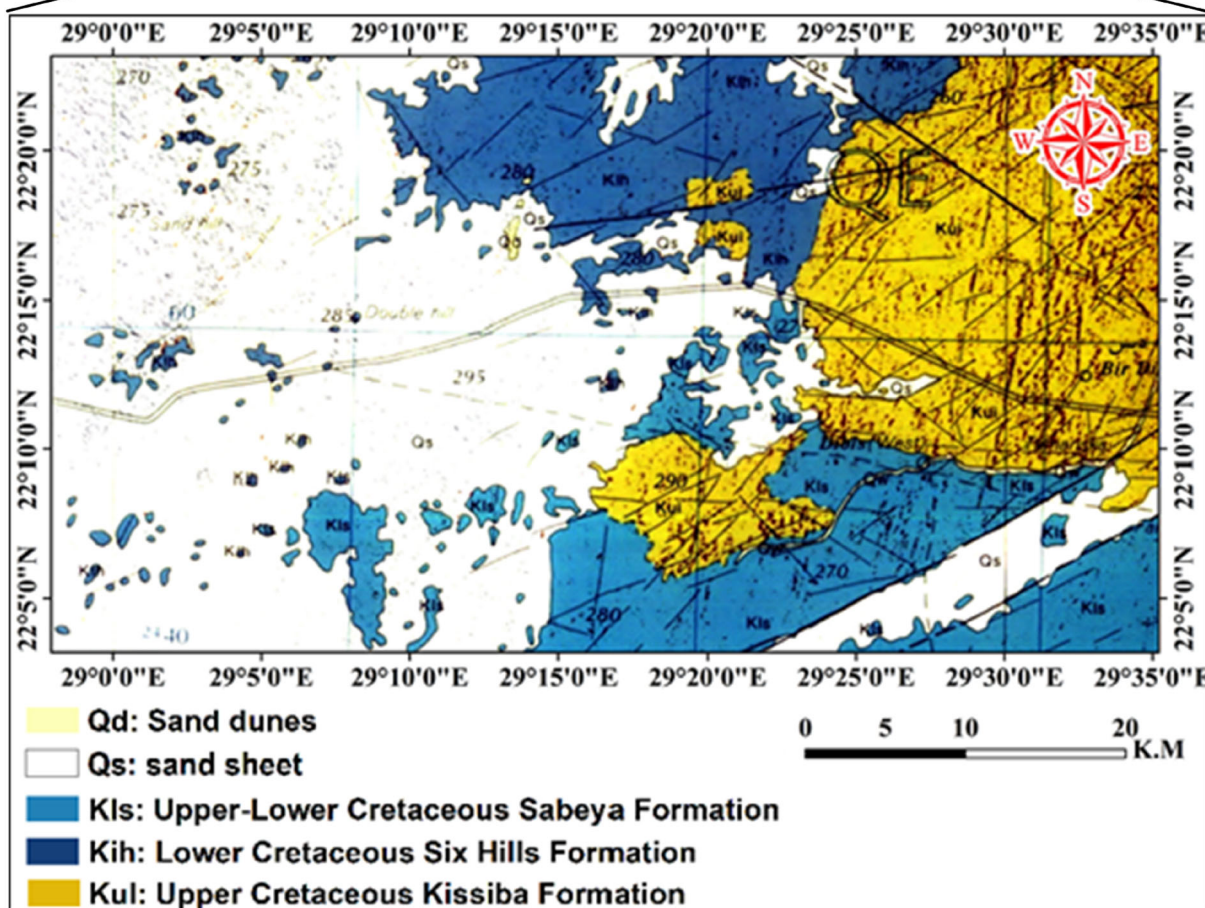
Magnetic Data Acquisition

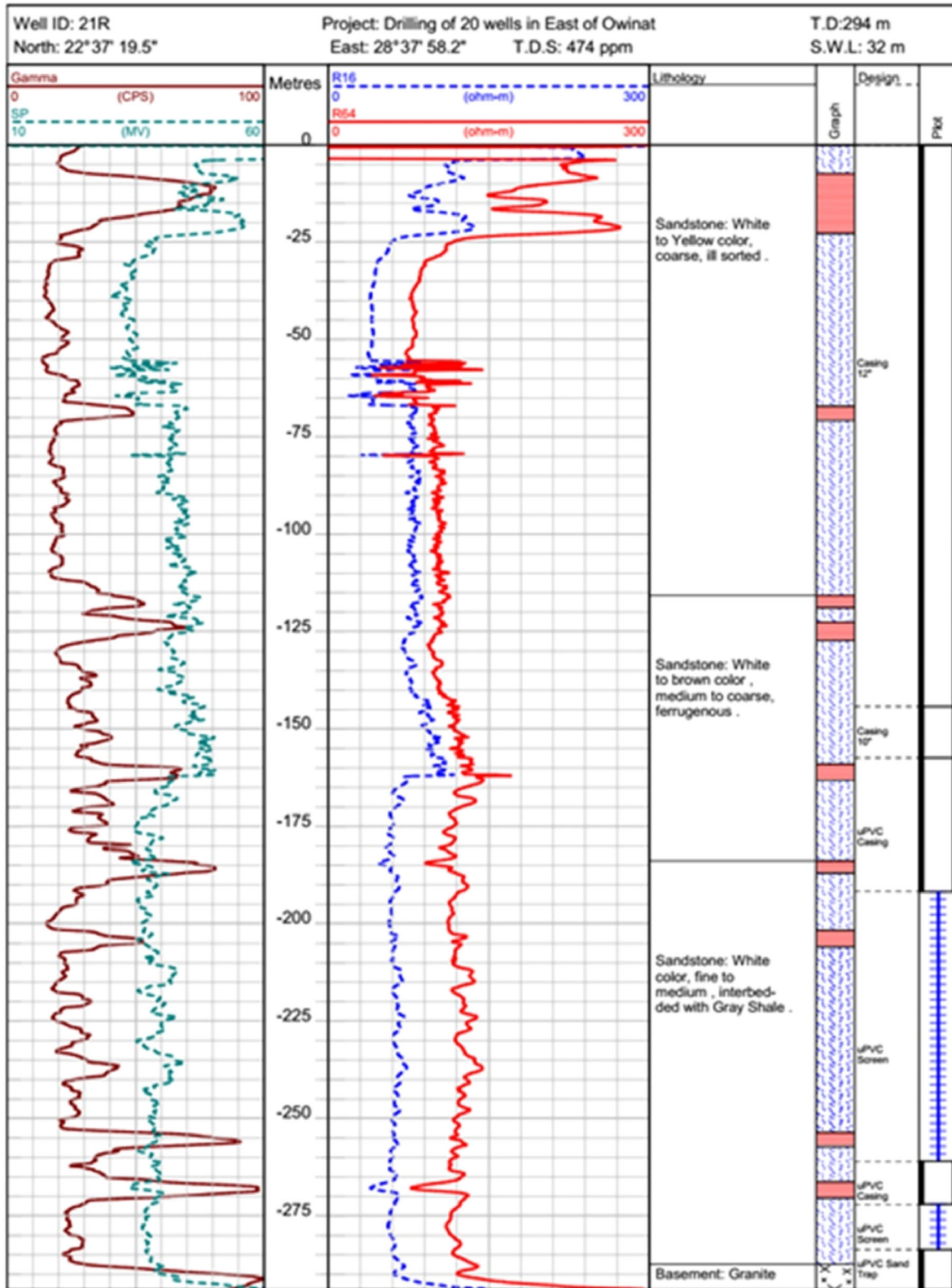
The area investigated was divided into a semi-regular grid with spacing of 500 m. The measurements were carried out using two magnetometer models: G856 proton magnetometer with 0.1 nT accuracy was used at the base station, and a Cesium magnetometer was used for field survey. Data correction included diurnal variations and International Geomagnetic Reference Field (IGRF) removal for preparing the total magnetic intensity (TMI) map (Fig. 3a). The south and central parts of the area show high magnetic values up to 40,045 nT, but the northern and eastern portions of the area exhibit smaller low and high magnetic variations having NW–SE and NE–SW trends.

(a)



(b)





◀ **Figure 2.** Well log of borehole 21R, and corresponding lithological description, in which layers with clay content exhibit high Gamma ray values.

Reduction to the Pole (RTP)

The resulting magnetic anomalies have characteristic shapes that depend on some factors such as strike and dip of bodies, their depth of burial and inclination, and declination of the inducing field where some distortion for the magnetic anomalies can occur because the area lies between the equator and pole (Baranov & Naudy, 1964). The reduced to magnetic pole (RTP) map shows a northward shift in the positions of most magnetic anomalies due to the elimination of the inclination of the magnetic field in this area (Fig. 3b). This results in a magnetic map where anomalies are located vertically above their sources. These magnetic anomalies indicate shallow magnetic sources due to the iron oxides in sandstone (ferruginous sandstone).

Magnetic Separation

Magnetic anomalies that result from shallow sources (residual anomalies) were separated from other effects that result from relatively deeper sources (regional anomalies). There are several analytical techniques by which the regional, as well as the residual, effects can be estimated.

Low- and High-Pass Filtering

In this study, we utilized Oasis Montaj (2015) for separation of regional component (low pass) and residual component (high pass) through low- and high-pass filtering. The power spectrum curve (Fig. 3c) was used to define the wavenumber (0.426 1/k unit). Figure 3c indicates that the deep source's depth was about 2.06 km, which represents the variation in the basement rocks. The depth of shallow sources was 0.484 km, which represents the contact between sedimentary and basement rocks. The residual magnetic component (high pass) indicates different anomalies of high and low amplitudes, which refer to the variation of ferruginous sandstone (Fig. 4a). The most commonly appearing trends of these anomalies were N–S and NE–SW. The regional magnetic map (low pass) shows a high

magnetic anomaly at the central portion of the area and low magnetic anomalies at the western and eastern portions (Fig. 4b). This low-pass map was used to construct a fault elements map (Fig. 4c); this map confirmed that the area is affected by different faults of N–S, NW–SE and NE–SW trends.

Magnetic Interpretation

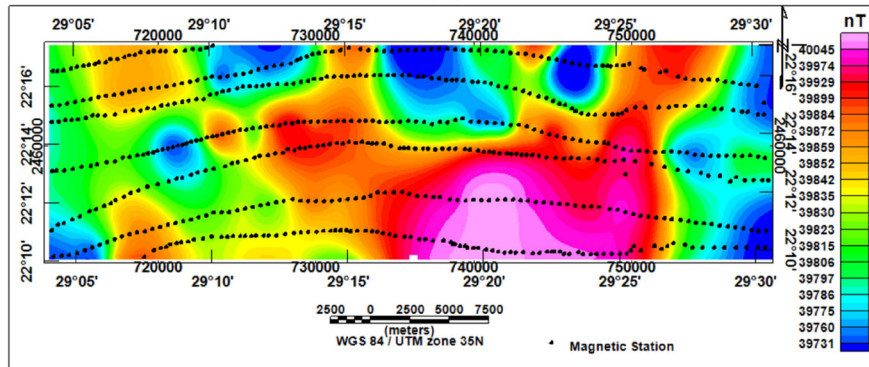
Euler Deconvolution

The depth to the top surface of magnetic sources that produce observed anomalies was estimated by the Euler deconvolution technique. We applied this technique using a structural index (SI) of 0, which is related to contact or step and window size of 250 m, where the SI is an exponential factor corresponding to the rate at which the field falls off with distance, for a source of a given geometry. The essential benefit of the interpretation of magnetic data is the mapping of basement relief. In other words, variations in thickness of the sedimentary cover reflect topographic changes or basement relief. The magnetic depths, derived from Euler's deconvolution, are plotted on a map to give Euler solutions for different depths where depths lower than 50 m represent the distribution of ferruginous sandstone, while most magnetic sources located at depths in the 400–700 m range are concentrated at the central part of the study area (Fig. 5). Most solutions have N–S, NW–SE, and NE–SW trends.

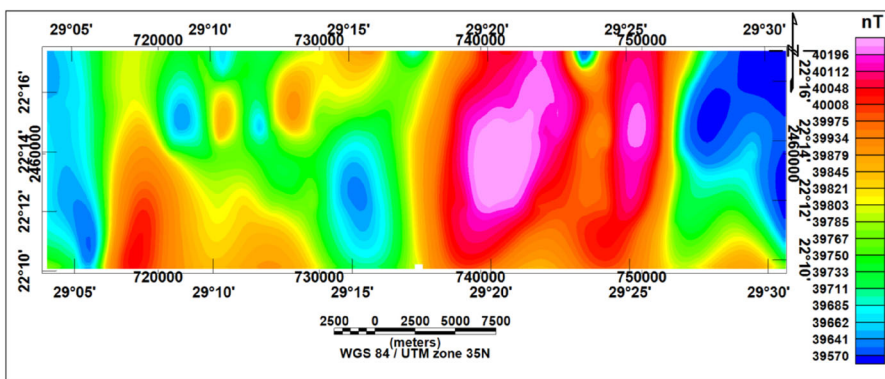
3D Magnetic Inversion

The 3D magnetic inversion was carried out using Oasis Montaj (2015) through GMSYS3D to estimate the depth of basement rocks according to Parker's algorithm (Parker, 1973). The 3D magnetic inversion used a smooth RTP map after removing the magnetic response from ferruginous sandstone as an observed map. The result of 3D magnetic inversion indicates that the observed and calculated maps were compatible (Fig. 6a–c), where the error map representing the difference between observed and calculated magnetic values shows variations ranging from – 12 to 13 nT (Fig. 6c). The depth of the basement surface varied between 384 and 1286 m (Fig. 6d); the 3D view of the elevation of the basement is shown in Figure 6e.

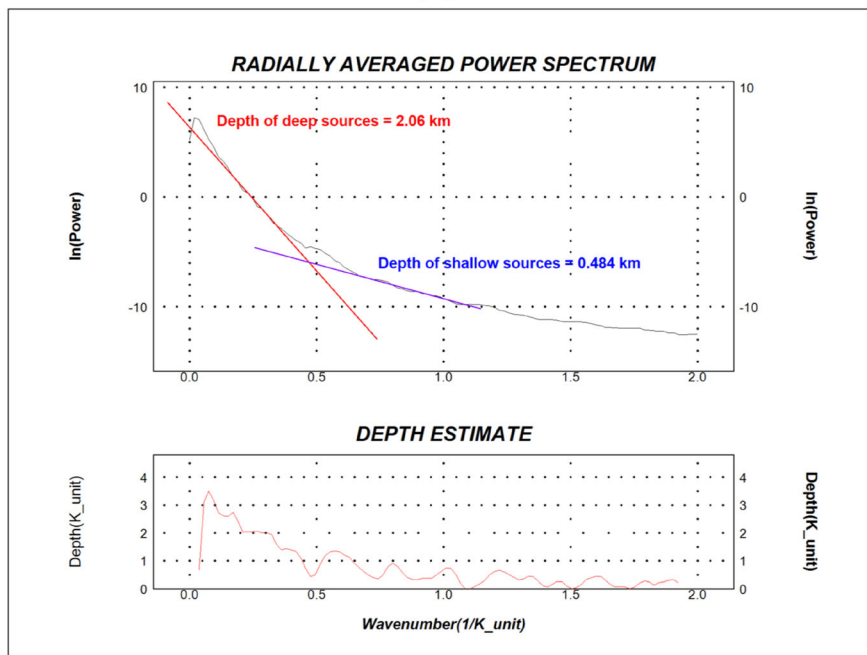
(a)



(b)



(c)



◀ **Figure 3.** (a) Total magnetic intensity (TMI) map. (b) Reduced to pole (RTP) map. (c) Power spectrum curve.

Geoelectrical Survey

Thirty sounding points (Fig. 7a) were chosen on a grid, where the spacing between every successive VES station was about 5000 m (Fig. 7). The maximum size of the current electrode dipole was 1400 m, and current electrode spacing (AB) was 1400 m ($AB/2 = 1.5\text{--}700$ m).

Interpretation of Geoelectrical Data

Quantitative interpretation of geoelectrical resistivity data aims to estimate true thicknesses and resistivities of successive subsurface geological units. We used two techniques for quantitative interpretation. The first was a graphical technique for determining the initial resistivity model. The second was an analytical method, based on the IPI2Win software (Bobachev et al., 2008), for improving the initial model and estimating the one-dimensional accurate resistivity profile versus depth (Bobachev et al., 2008). A result is generally obtained, after some iterations, through a least-square fit between calculated apparent resistivity values and observed apparent resistivity values obtained from field measurements. Calibration of the geoelectrical data recorded during the present campaign was performed using the result of a VES station carried out beside borehole 21R, which was drilled outside the study area as shown in Figure 7b. The sounding points were interpreted in terms of actual resistivities and depths for the encountered layers constituting the study area's shallow section. The interpretations of all VES stations are presented as supplementary material.

Geoelectrical Cross Sections

Three sections were established to detect the subsurface geological situation of the study area. These sections give an ideal picture of the continuity or discontinuity of the lithologic units and clearly highlight the geological structures that affect the

area. The first section along profile P1–P1' (Fig. 8a) was established including soundings from VES 1 to VES 10; this section is dissected by four fault elements denoted F1, F2, F3, and F4. The second cross section along profile P2–P2' (Fig. 8b) was constructed including soundings from VES 11 to VES 20; this section is dissected by two fault elements denoted F1 and F2. The third geoelectrical cross section along P3–P3' (Fig. 8c) includes soundings from VES 21 to VES 30; this section is dissected by three fault elements denoted F2, F3, and F4.

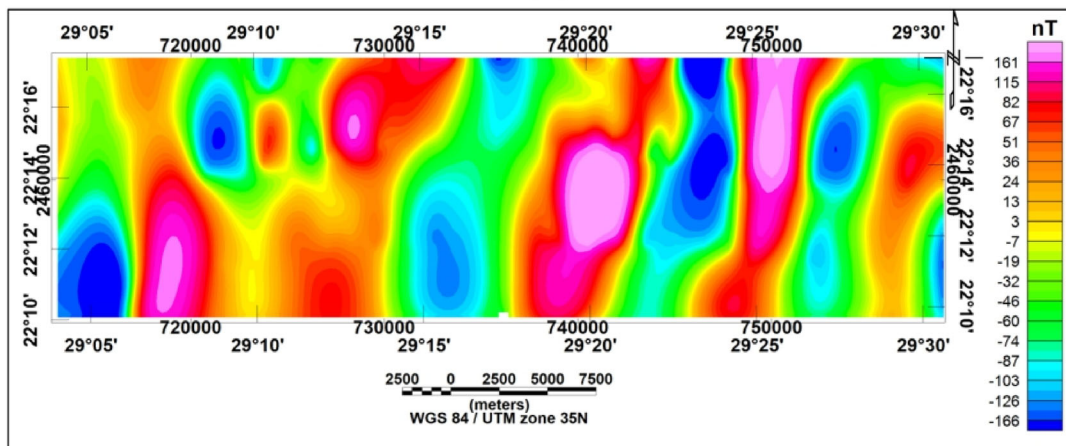
The presence of five geoelectrical layers characterizes the geoelectrical cross sections. The first layer exhibits moderate resistivity values ranging from 188 at VES27 to 1864 Ω m at VES16 and thickness ranging from 0.8 at VES27 to 2.6 m at VES3 corresponding to gravel and sand. The second layer represents high resistivity values corresponding to ferruginous sandstone with resistivity values ranging from 1825 Ω m at V30 to 7706 Ω m at V16 and thickness ranging from 2.8 m at V23 to 9.1 m at V15. The third layer reflects relatively low resistivity values ranging from 93 Ω m at V7 to 585 Ω m at V20, which are indicative of clay, and thickness ranging from 7 m at V7 to 22 m at V24. The fourth layer represents a high resistive layer corresponding to dry sandstone, with resistivity values ranging from 933 Ω m at V8 to 6053 Ω m at V13 and thickness ranging from 20 m at V29 to 39.2 m at V24. The fifth layer has resistivities between 116 and 252 Ω m; lithologically, this layer is composed of sandstone with clay intercalation. It is important to mention that this fifth layer is the Nubian sandstone aquifer (NSA) in the area, which contains freshwater according to borehole 21R, where the TDS was 474 ppm. The aquifer parameters are summarized in the next section.

RESULTS

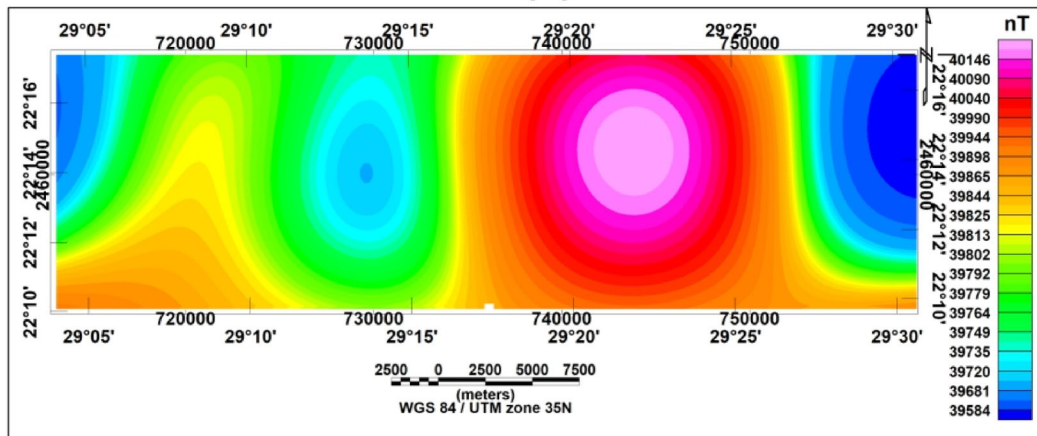
Depth Map of NSA

The depth of the upper surface of the NSA was estimated through interpretation of geoelectrical data. The depth to the aquifer (Fig. 9a) was 27 m at the SW and SE parts of the study area and 65 m at the northeastern, central, and western parts.

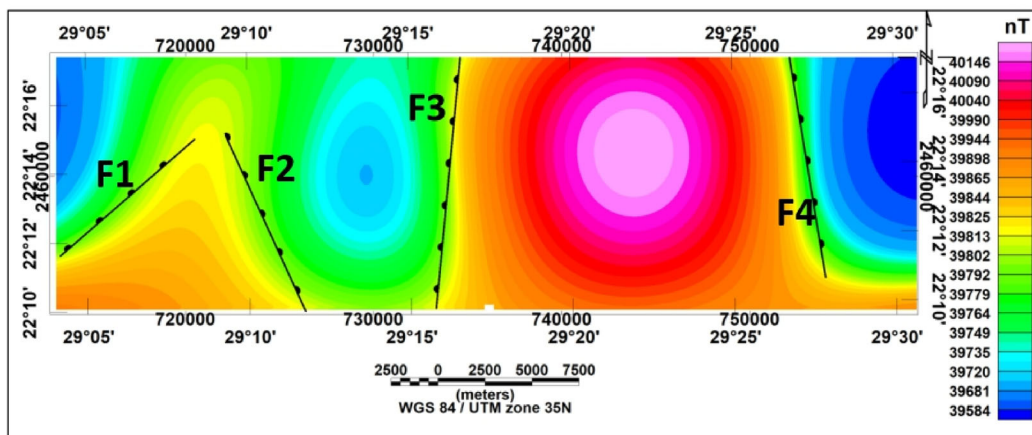
(a)



(b)



(c)



◀ **Figure 4.** (a) Residual map obtained by high-pass filtering of reduced to pole magnetic data. (b) Regional map obtained by high-pass filtering of reduced to pole magnetic data. (c) Faults interpreted from the regional magnetic map.

Thickness Map of NSA

The thickness of the NSA was determined based on its top surface determined from the geoelectrical data and based on its bottom surface (as well as the surface basement rocks) determined from the magnetic data. The aquifer thickness was estimated as 299 m in the central part of the study area and 1169 m in the western and eastern parts (Fig. 9b).

Iso-Resistivity Map of NSA

The resistivity of the aquifer derived from interpretation of the geoelectrical data ranged from 135 Ω m (at the west of the central part and north-eastern part) to 235 Ω m (at the eastern, central, and western parts) (Fig. 9c).

Salinity Map (TDS) of NSA

The salinity of water was calculated from the Archie (1942) equation for total dissolved salt (TDS), whereby resistivities of water can be estimated from bulk resistivity values of NSA (ρ_b) from VES interpretation and from resistivity of water (ρ_w) from borehole 21R according to the following equations:

$$f = \frac{\rho_b}{\rho_w} \tag{1}$$

where f is the formation factor dependent on porosity (ϕ), thus (Winsauer et al., 1952):

$$f = \frac{a}{\phi^m} \tag{2}$$

where a is a constant taken as 0.62 for soft deposits.

By using $f = 5.4$ (Aweto, 2013) in Eq. 1, TDS in mg/l was calculated as:

$$\text{TDS (ppm)} = 0.64 \times \text{EC} \tag{3}$$

where $\text{EC} = \frac{10,000}{\rho_w} \mu\text{S/cm}$, and so Eq. 3 becomes:

$$\text{TDS(PPM)} = \frac{10,000}{\rho_w} \times 0.64 \tag{4}$$

The salinity map for NSA exhibits TDS values ranging from 143 ppm at the eastern, western, and central parts of the area to 244 ppm at most of the

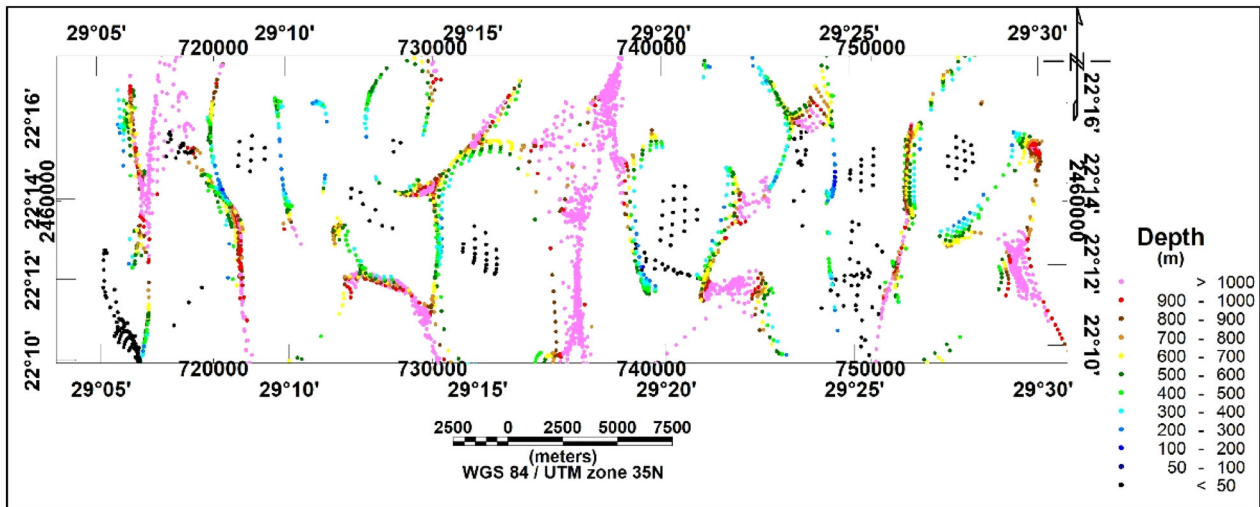


Figure 5. Euler deconvolution solutions using structural index (SI) = 0.

study area indicating high-quality freshwater (Fig. 9d).

DISCUSSION

The study area lies in the southern part of Egypt, where two geophysical tools were applied to delineate the NSA. The results of the two geophysical tools are compatible, namely that the study area is dissected by four faults based on the magnetic and geoelectrical data. The locations of these faults were confirmed by the two methods to be at shallow and deep levels. The lithology of borehole 21R indicates 7.5 m thick sandstone overlain by 15 m thick clay, sandstone intercalated with clay to a depth of 290,

Figure 7. (a) Location map of VES measurements. (b) Interpretation of test VES measured beside borehole 21R for correlation.

and water table at a depth of 32 m. These results are compatible with the geoelectrical data.

The resistivity values of the NSA vary between 135 and 235 Ω m. These indicate freshwater quality, as supported by maximum TDS in borehole 21R TDS of 474 ppm. The resistivity values also indicate that the salinity is 142–242 part per million. Based on the depth map, isopach map, iso-resistivity, and TDS maps of the aquifer, the planning for drilling outlines zone A as the first priority because it is shallower with high thickness and high resistivity

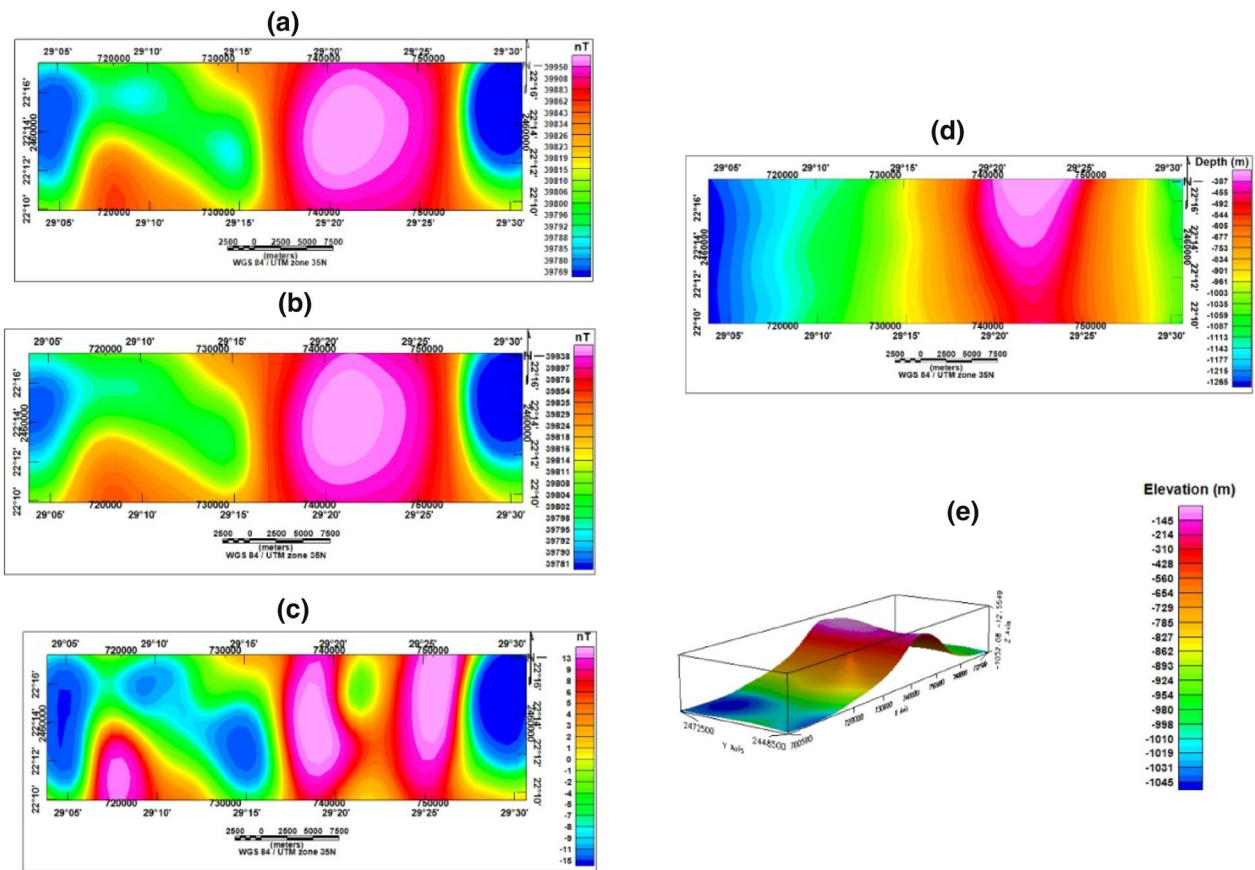
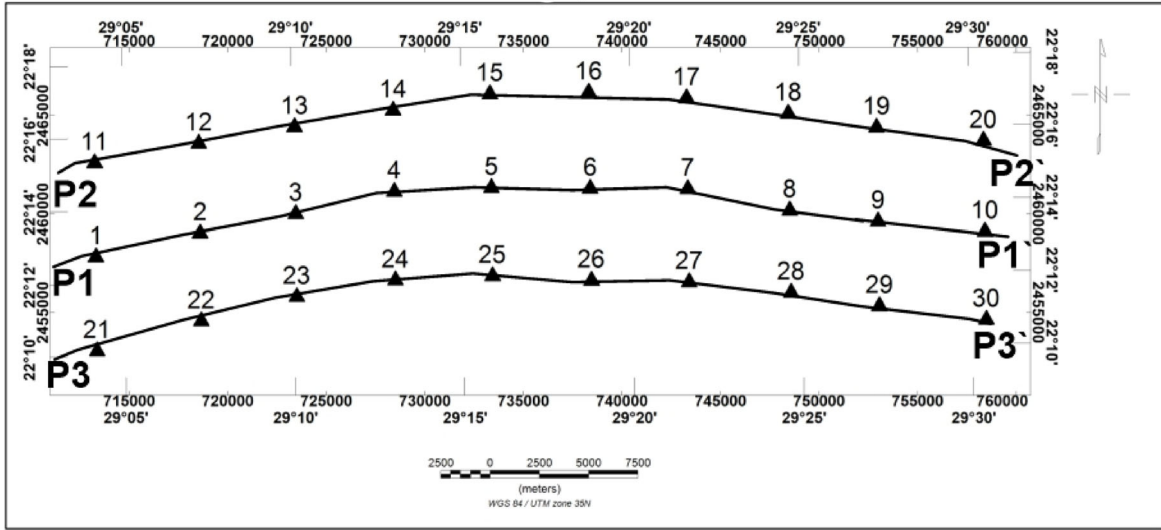
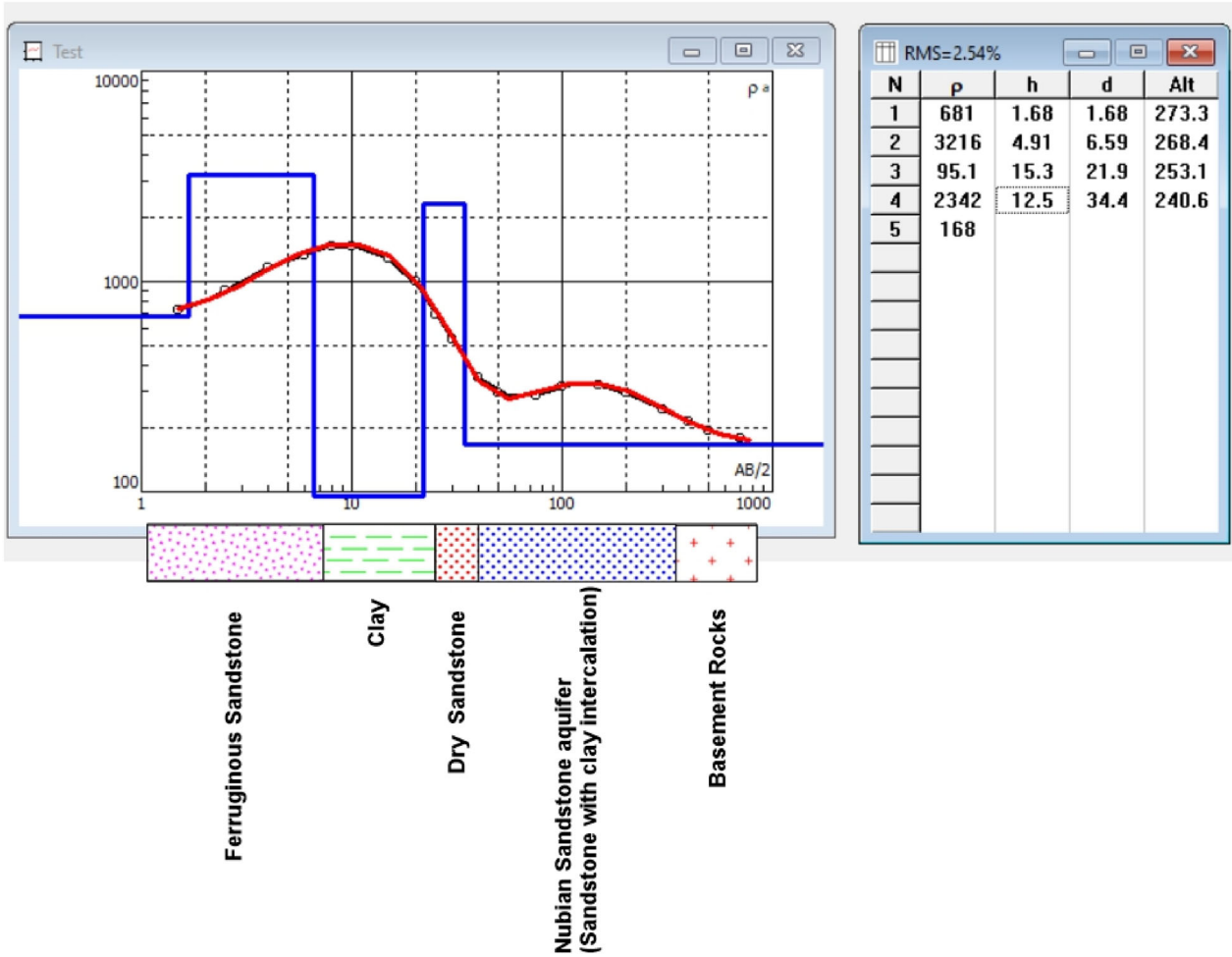


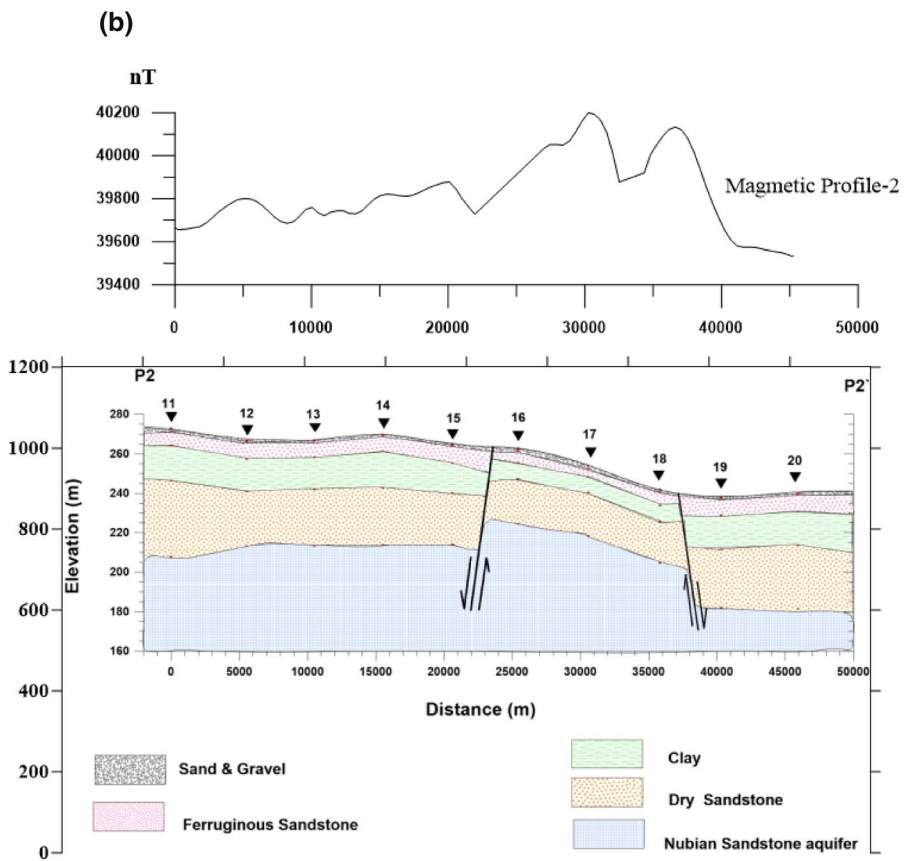
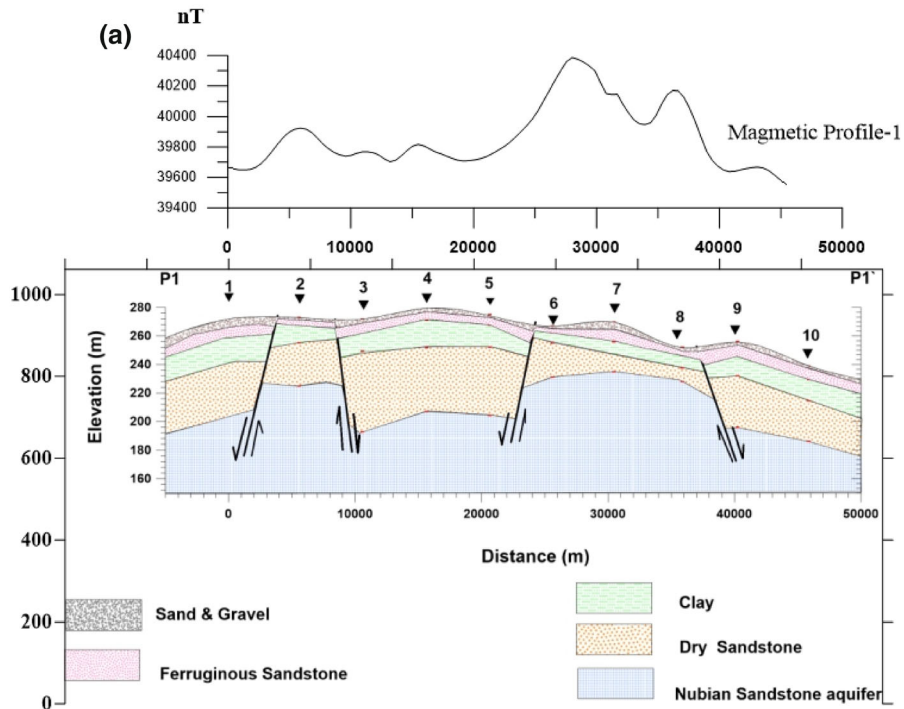
Figure 6. Output of GMSYS3D. (a) Observed magnetic map. (b) Calculated magnetic map. (c) Error map. (d). Depth to basement rocks. (e) 3D view of elevation of basement surface.

(a)



(b)





◀ **Figure 8.** (a) Geoelectrical cross section along profile P1–P1' coupled with magnetic profile. (b) Geoelectrical cross sections along profile P2–P2' coupled with magnetic profile. (c) Geoelectrical cross section along profile P3–P3' coupled with magnetic profile.

(more freshwater), and zone B as the second priority because it is deeper with high thickness and high resistivity values (Fig. 9e).

CONCLUSIONS

The results of using two geophysical tools indicate that the study area consists of five layers (gravel and sandstone, ferruginous sandstone, clay, dry sandstone, and Nubian sandstone aquifer composed of sandstones intercalated with clay). The depth of the Nubian sandstone aquifer ranges from 27 to 65 m. Its thickness ranges from 299 to 1169 m. The groundwater is freshwater based on its resistivities ranging from 135 to 235 Ω m and based on its TDS ranges from 142 to 242 ppm. The study area is affected by faults of N–S, NE–SW, and NW–SE trends. The depth of basement rocks ranges from 384 to 1286 m.

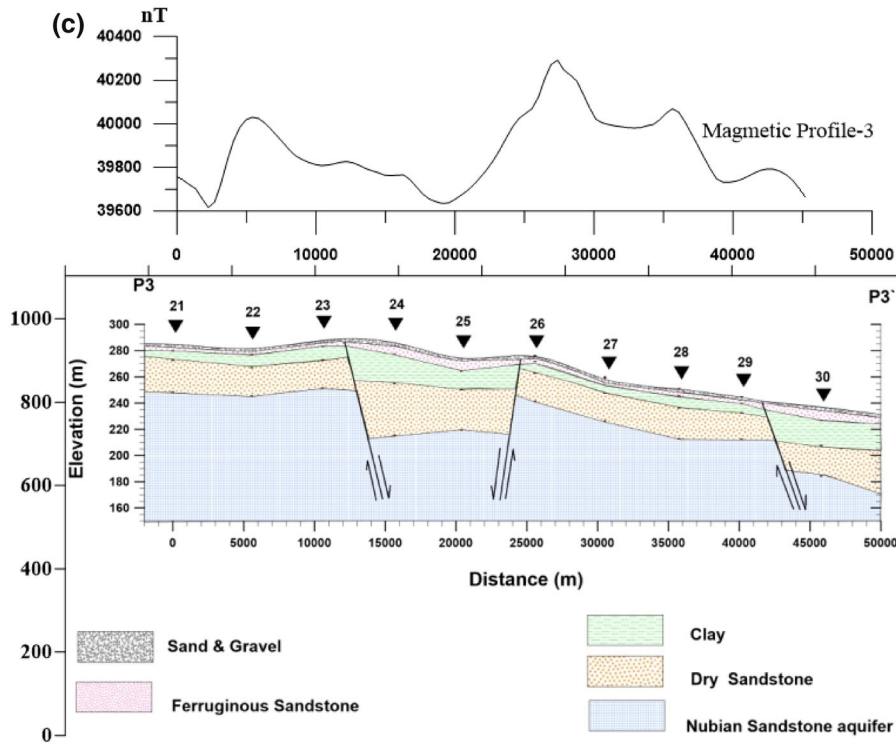


Figure 8. continued.

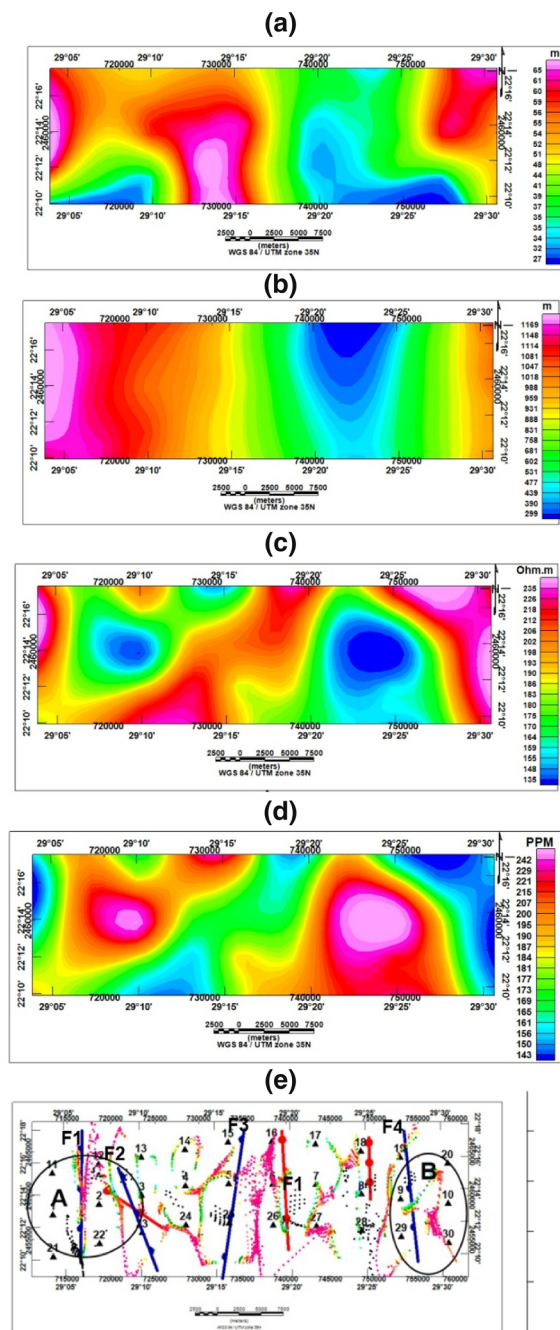


Figure 9. Maps of the Nubian sandstone aquifer: (a) Depth map. (b) Isopach map. (c) Iso-resistivity map. (d) Salinity (in ppm) map. (e) Summary map. In (e), blue lines are interpreted from Euler deconvolution of the magnetic data and depict faults that affect the basement, whereas red lines depict faults interpreted from VES data and correlated across the three profiles. Priority areas outlined for drilling work are marked A and B.

ACKNOWLEDGMENTS

The authors extend their sincere gratitude and appreciation to the Research Institute for Groundwater (RIGW) for their help in achieving this paper. Likewise, they are grateful to the reviewers who reviewed this research for publication.

SUPPLEMENTARY INFORMATION

The online version contains supplementary material available at <https://doi.org/10.1007/s11053-021-09937-y>.

REFERENCES

- Al Temamy, A. M. M., & Barseem, M. S. M. (2010). Structural impact on the groundwater occurrence in the Nubia sandstone aquifer using geomagnetic and geoelectrical techniques, northwest Bir Tarfawi, east El Oweinat area, Western Desert. *EGS Journal*, 8(1), 47–63.
- Araffa, S. A. S. (2013). Delineation of under groundwater aquifer and subsurface structures on north Cairo Egypt, used integrated interpretation of magnetic, gravity, and geoelectrical data. *Geophysical Journal International*, 192(1), 94–112.
- Araffa, S. A. S., Abdelazium, M., Sabet, H. S., & Al Dabour, A. (2021). Hydrogeophysical investigation at El Moghra area, North Western Desert, Egypt. *Environmental Earth Sciences*, 80(2), 55–80.
- Araffa, S. A. S., Alrefae, H. A., & Nagy, M. (2020). Potential of groundwater occurrence using geoelectrical and magnetic data: A case study from south Wadi Hagul area, the northern part of the Eastern Desert, Egypt. *Journal of African Earth Sciences*, 172, 103970.
- Araffa, S. A. S., El Shayeb, H. M., Abu-Hashish, M. F., & Hassan, N. M. (2015). Integrated geophysical interpretation for delineating the structural elements and under groundwater aquifers at the central part of Sinai Peninsula. *Arabian Journal of Geosciences*, 8, 7993–8007.
- Archie, G. E. (1942). The electrical resistivity log as an aid in determining some reservoir characteristics. *Transactions of the AIME*, 146, 54–62.
- Attia, O. E. A., & Hussien, K. H. (2015). Sedimentological characteristics of continental sabkha, south Western Desert, Egypt. *Arabian Journal of Geosciences*, 8, 7973–7991.
- Aweto, K. E. (2013). Resistivity methods in hydrogeophysical investigation for groundwater in Aghalokpe, Western Niger Delta. *Global Journal of Geological Science*, 11, 47–55.
- Baranov, V., & Naudy, H. (1964). Numerical calculation of the formula of reduction to the magnetic pole. *Geophysics*, 29, 67–79.
- Bobachev, A., Modin, I., & Shevinin, V. (2008). IPI2Win V2.0: user's Guide. Moscow State University, Moscow. <http://geophysics.geol.msu.ru/ipi2win.htm>.
- CONOCO. (1987). Geological map of Egypt, scale 1:500,000.
- El Osta, M. M. (2006). *Evaluation and management of groundwater in East El Oweinat Area, Western Desert, Egypt*. Ph.D. Thesis. Geology Department, Faculty of Science, Minufiya University.

- EL-Badrawy, H. T., Araffa, S. A. S., & Gabr, A. F. (2021). Application of the multi-potential geophysical techniques for under groundwater evaluation in a part of central Sinai Peninsula Egypt. *Acta Geodynamica Et Geomaterialia*, 18(1), 61–70.
- Elbarbary, S., Araffa, S. A. S., El-Shahat, A., AbdelZaher, M., & Khedher, K. M. (2021). Delineation of water potentiality areas at Wadi El-Arish, Sinai, Egypt, using hydrological and geophysical techniques. *Journal of African Earth Sciences*, 174, 104056.
- Goldman, M., & Neubauer, F. M. (1994). Groundwater exploration using integrated geophysical techniques. *Survey in Geophysics*, 15, 331–361.
- Hendriks, F., Luger, P., Bowitz, J., & Kallenbach, H. (1987). Evolution of the depositional environments of the SE-Egypt during the cretaceous and lower tertiary. Subproject A3 "Sedimentary basin of Southern Egypt." *Berl. Geowiss.*, 75, 49–80.
- Issawi, B. (1971). The geology of Darb El-Arbeain, Western Desert, Egypt. *Annals of the Geological Survey of Egypt*, 1, 53–92.
- Issawi, B. (1973). Nubia sandstone type section. *Bulletin AAPG*, 57, 741–745.
- Klitzsch, E. (1978). Geologische Bearbeitung Sudwest-Agyptens. *Geologische Rundschau*, 67, 509.
- Klitzsch, E., & Lejal-Nicol, A. (1984). Flora and Fauna from Strata in Southern Egypt and Northern Sudan. *Berliner Geowissenschaftliche Abhandlungen*, 50, 47–79.
- Masoud, M. H., Schneider, M., & El Osta, M. M. (2013). Recharge flux to the Nubian Sandstone aquifer and its impact on the present development in southwest Egypt. *Journal of African Earth Sciences*, 85, 115–124.
- Oasis Montaj Programs. (2015). Geosoft mapping and processing system: Version 8.3.2 (HJ), Inc Suit 500, Richmond St. West Toronto, ON Canada N5S1V6.
- Parker, R. L. (1973). The rapid calculation of potential anomalies. *Geophysical Journal International*, 31(4), 447–455.
- Winsauer, W. O., Shearin, H. M., Jr., Masson, P. H., & Williams, M. (1952). Resistivity of brine saturated sands in relation to pore geometry. *American Association of Petroleum Geologists Bulletin*, 36(2), 253–277.